



**HAL**  
open science

## **La<sub>1-x</sub>(Sr, Na, K)<sub>x</sub>MnO<sub>3</sub> perovskites for HCHO oxidation: the role of oxygen species on the catalytic mechanism**

Yin Xu, Jérémy Dhainaut, Jean-Philippe Dacquin, Anne-Sophie Mamede, Maya Marinova, Jean-Francois Lamonier, Herve Vezin, Hui Zhang, Sébastien Royer

### ► To cite this version:

Yin Xu, Jérémy Dhainaut, Jean-Philippe Dacquin, Anne-Sophie Mamede, Maya Marinova, et al.. La<sub>1-x</sub>(Sr, Na, K)<sub>x</sub>MnO<sub>3</sub> perovskites for HCHO oxidation: the role of oxygen species on the catalytic mechanism. Applied Catalysis B: Environmental, In press, 287, pp.119955. 10.1016/j.apcatb.2021.119955 . hal-03138753

**HAL Id: hal-03138753**

**<https://hal.univ-lille.fr/hal-03138753>**

Submitted on 11 Feb 2021

**HAL** is a multi-disciplinary open access archive for the deposit and dissemination of scientific research documents, whether they are published or not. The documents may come from teaching and research institutions in France or abroad, or from public or private research centers.

L'archive ouverte pluridisciplinaire **HAL**, est destinée au dépôt et à la diffusion de documents scientifiques de niveau recherche, publiés ou non, émanant des établissements d'enseignement et de recherche français ou étrangers, des laboratoires publics ou privés.

# Journal Pre-proof

La<sub>1-x</sub>(Sr, Na, K)<sub>x</sub>MnO<sub>3</sub> perovskites for HCHO oxidation: the role of oxygen species on the catalytic mechanism

Yin Xu (Investigation) (Formal analysis) (Data curation) (Writing - original draft), Jérémy Dhainaut (Writing - review and editing) (Supervision), Jean-Philippe Dacquin (Supervision), Anne-Sophie Mamede (Formal analysis) (Investigation), Maya Marinova (Formal analysis) (Investigation), Jean-François Lamonier (Supervision), Hervé Vezin, Hui Zhang (Supervision) (Funding acquisition), Sébastien Royer (Supervision) (Funding acquisition)



PII: S0926-3373(21)00081-3

DOI: <https://doi.org/10.1016/j.apcatb.2021.119955>

Reference: APCATB 119955

To appear in: *Applied Catalysis B: Environmental*

Received Date: 17 September 2020

Revised Date: 27 January 2021

Accepted Date: 28 January 2021

Please cite this article as: Xu Y, Dhainaut J, Dacquin J-Philippe, Mamede A-Sophie, Marinova M, Lamonier J-François, Vezin H, Zhang H, Royer S, La<sub>1-x</sub>(Sr, Na, K)<sub>x</sub>MnO<sub>3</sub> perovskites for HCHO oxidation: the role of oxygen species on the catalytic mechanism, *Applied Catalysis B: Environmental* (2021), doi: <https://doi.org/10.1016/j.apcatb.2021.119955>

This is a PDF file of an article that has undergone enhancements after acceptance, such as the addition of a cover page and metadata, and formatting for readability, but it is not yet the definitive version of record. This version will undergo additional copyediting, typesetting and review before it is published in its final form, but we are providing this version to give early visibility of the article. Please note that, during the production process, errors may be discovered which could affect the content, and all legal disclaimers that apply to the journal pertain.

© 2020 Published by Elsevier.

$\text{La}_{1-x}(\text{Sr}, \text{Na}, \text{K})_x\text{MnO}_3$  perovskites for HCHO oxidation: the role of  
oxygen species on the catalytic mechanism

Yin Xu,<sup>a,b,‡</sup> Jérémy Dhainaut,<sup>b\*</sup> Jean-Philippe Dacquin,<sup>b</sup> Anne-Sophie Mamede,<sup>b</sup>  
Maya Marinova,<sup>c</sup> Jean-François Lamonier,<sup>b</sup> Hervé Vezin,<sup>d</sup> Hui Zhang,<sup>a\*</sup> Sébastien  
Royer<sup>b</sup>

<sup>a</sup> Department of Environmental Science and Engineering, Hubei Environmental Remediation Material Engineering Technology Research Center, Wuhan University, Wuhan 430079, China

<sup>b</sup> Univ. Lille, CNRS, Centrale Lille, Univ. Artois, UMR 8181 - UCCS - Unité de Catalyse et Chimie du Solide, F-59000 Lille, France

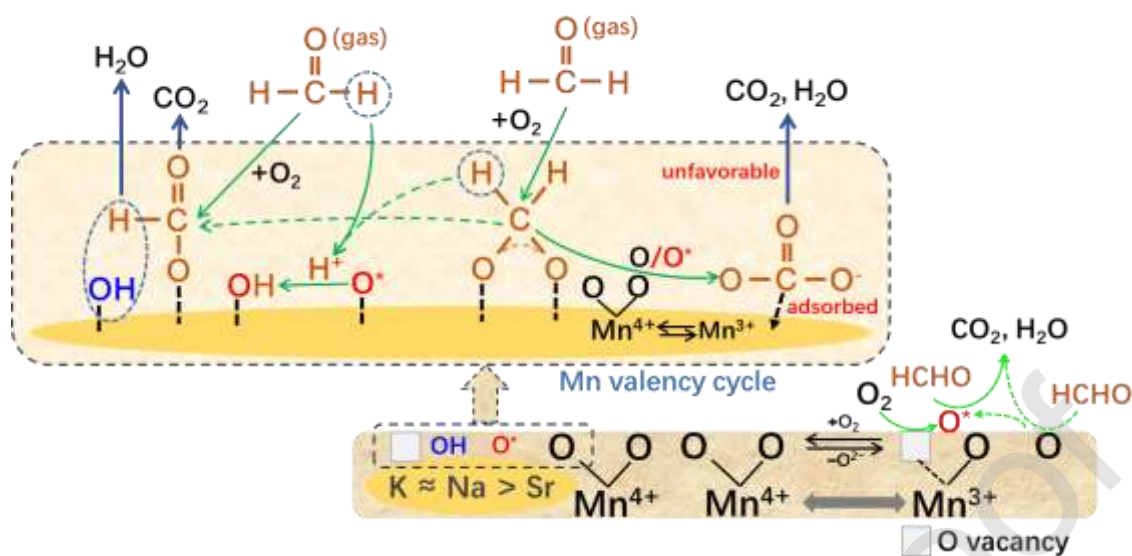
<sup>c</sup> Univ. Lille, CNRS, INRA, Centrale Lille, Univ. Artois, FR 2638 - IMEC - Institut Michel-Eugène Chevreul, F-59000 Lille, France

<sup>d</sup> Univ. Lille, CNRS UMR 8516 - LASIRE - Laboratoire Avancé de Spectroscopie pour les Interactions la Réactivité et l'Environnement, F-59000 Lille, France

\*Corresponding Authors: H. Zhang (email. eeng@whu.edu.cn); J. Dhainaut (email. jeremy.dhainaut@univ-lille.fr)

‡ Present adress: School of Resources and Environmental Science, Hubei University, Wuhan, 430062, China

## Graphical abstract



## Highlights

- A-site substituted perovskites used for catalytic oxidation of formaldehyde.
- The catalytic mechanism was investigated and a pathway is proposed.
- LKMO and LNMO perovskites present TOFs in the range of noble metal-based catalysts.

## Abstract:

A-site substituted perovskites were prepared and evaluated for formaldehyde oxidation. Based on the T<sub>50</sub>, the catalytic activity ranking was: La<sub>0.8</sub>K<sub>0.2</sub>MnO<sub>3</sub> > La<sub>0.8</sub>Na<sub>0.2</sub>MnO<sub>3</sub> (LNMO) > La<sub>0.8</sub>Sr<sub>0.2</sub>MnO<sub>3</sub> > LaMnO<sub>3</sub>. This improved activity is associated to (i) higher density of surface adsorption sites and (ii) higher bulk oxygen mobility. Stability tests, under humid and dry conditions, were also conducted. In dry conditions, a gradual deactivation of the substituted perovskites (from 50% to 15% HCHO conversion after 64 h, LNMO) was correlated to the loss of surface-active

oxygen species and high-valence  $\text{Mn}^{4+}$ . Besides, the presence of abundant adsorbed oxidation intermediates likely inhibited the reactivation of the catalyst surface. This inhibition was limited when humidity was added in the stream of gas, thus lowering the catalysts' deactivation, demonstrating the importance of  $-\text{OH}$  surface groups on the catalyst surface in the oxidation mechanism. Consequently, this work highlights the design of perovskite-based catalysts with superior oxidation properties.

**Keywords:** Formaldehyde oxidation; Perovskite; A-site substitution; Deactivation; Oxidation mechanism.

## 1. Introduction

Air pollution represents an ever-growing threat for public health and is targeted as a high priority by the World Health Organization. In particular, indoor air pollution is categorized as one of the five most harmful environmental factors for human health [1]. While particulate pollution represents the main risk factor, volatile organic compounds (VOCs) are also of high concern. Formaldehyde (HCHO), classified as carcinogenic to humans (group 1), is among the most significant VOCs, due to its wide use in resins and insulation, but also in plastics, coatings, and textiles as a disinfectant and preservative [2]. Moreover, its gradual release from furniture can take many years, with indoor concentrations in the ppb to ppm level. Global exposure to formaldehyde was increased by 21.5% between 2007 and 2017, representing an estimated 1000 premature deaths annually [1].

Low temperature catalytic oxidation is considered as an attractive technology for indoor air purification owing to a durable abatement efficiency, low energy needs, and simple installation. It avoids regular adsorbents regeneration, and additional operating and equipment costs of plasma- and photocatalytic-based oxidation technologies. Currently, the catalytic materials used for HCHO oxidation are based on supported noble metals (Pd, Pt, Rh, Ag and Au) [3], as they usually exhibit higher catalytic activity than transition metal oxides. Nevertheless, the reduction of noble metals use is of strategic importance due to their limited availability. Therefore, the development of catalysts based on transition metal oxides remains highly attractive [4].

Ideal perovskite structure is described as cubic or nearly-cubic with a general chemical formula  $ABX_3$ , where A and B are cations – such as transition metals – and X is usually oxygen. Perovskites are recognized for their high thermal stability, their exceptional composition versatility, and their tailored redox properties, favorable for a

broad range of catalytic applications up to the industrial scale [5]. More specifically in the domain of air purification, perovskite oxides built from B-site cations with a reducible transition metal (*i.e.* Co, Mn) are widely used for the catalytic oxidation of hydrocarbons [6], CH<sub>4</sub> [7], stearic acid [8], and NO [9]. Moreover, partial substitution of A-site cations with lower valence elements was suggested to introduce oxygen vacancies, facilitating oxygen transfer and thus increasing oxygen mobility [7,10].

Alkali ions have gained a lot of attention in the past few decades due to their promoting effect on many important heterogeneous catalytic reactions. For example, the addition of an alkali ion (Na<sup>+</sup> or K<sup>+</sup>) is beneficial to the synthesis of ammonia [11], olefin production [12], and conversion of CO<sub>2</sub> to gasoline-range (C<sub>5</sub>-C<sub>11</sub>) hydrocarbons [13]. Furthermore, catalysts based on noble metals and doped with alkali ions have shown higher performances for the oxidation of several VOCs, including HCHO [14-17]. Notably, impregnation of Na<sup>+</sup> on Pt/TiO<sub>2</sub> catalyst surface decreases significantly the activation energy for HCHO oxidation through the stabilization of highly dispersed PtO(OH)<sub>x</sub>-Na<sup>+</sup> species [14]. Immersion of Pt/TiO<sub>2</sub> catalysts into a NaOH solution also led to improved activity for HCHO oxidation [17]. This improvement was correlated to the presence of additional surface OH<sup>-</sup> species, leading to improved HCHO adsorption capacity. Similar observations were reported in the case of Na<sup>+</sup>-modified Pd/TiO<sub>2</sub> catalyst [15] and K<sup>+</sup>-modified Ag/Co<sub>3</sub>O<sub>4</sub> catalyst [16]. While alkali ions effectively promote HCHO oxidation when using noble metal-based catalysts, only a few studies reported noble metal-free catalysts doped with alkali ions for the oxidation of HCHO [18-20].

Perovskite materials with partial substitution of their A-site element with alkali and alkaline earth cations have been already applied to environmental catalytic reactions [21-23]. However, no such substituted perovskite has been evaluated for

formaldehyde oxidation. In this work, a series of A-site partially substituted perovskites  $\text{La}_{0.8}\text{A}'_{0.2}\text{MnO}_3$  (A = Na, K, Sr) were prepared and compared to the reference  $\text{LaMnO}_3$  perovskite. Emphasis was given to the understanding of the influence of lower valence elements on the surface and bulk properties of the perovskite-based materials. Therefore, all materials were thoroughly characterized by XRD,  $\text{N}_2$  physisorption, ICP, XPS, FTIR, HR-STEM,  $\text{H}_2$ -TPR,  $\text{O}_2$ -TPD, and EPR, and comparatively investigated for the catalytic oxidation of HCHO at mild temperature. The long-term stability of the most active catalysts,  $\text{La}_{0.8}\text{K}_{0.2}\text{MnO}_{3.15}$  and  $\text{La}_{0.8}\text{Na}_{0.2}\text{MnO}_{3.15}$ , was further evaluated in the presence or absence of humidity.

## 2. Experimental

### 2.1. Materials preparation

All samples were prepared starting from metal nitrate precursors:  $\text{La}(\text{NO}_3)_3 \cdot 6\text{H}_2\text{O}$  ( $\geq 99.0\%$ ) from Sigma-Aldrich,  $\text{Mn}(\text{NO}_3)_2 \cdot x\text{H}_2\text{O}$  (98.0%) from Aldrich,  $\text{NaNO}_3$  (+99%) from Acros,  $\text{KNO}_3$  ( $\geq 99.0\%$ ) and  $\text{Sr}(\text{NO}_3)_2$  ( $\geq 99.0\%$ ) from Fluka, and citric acid (+99.5%) from Alfa Aesar.

$\text{LaMnO}_3$  perovskite has been prepared according to the procedure described elsewhere [4]. The maximum temperature applied for the thermal treatment was lowered to 650 °C. This reference is labelled LMO. A similar procedure was applied for the synthesis of alkali- and alkaline earth-substituted perovskites, with  $(n_{\text{A}} + n_{\text{Mn}} + n_{\text{La}})/n_{\text{citric acid}} = 1$ ,  $(n_{\text{A}} + n_{\text{La}})/n_{\text{Mn}} = 1$ , and  $n_{\text{A}}/n_{\text{La}} = 0.25$  (A representing either K, Na, or Sr). In a typical synthesis, appropriate amounts of alkali or alkaline earth nitrate, manganese nitrate and lanthanum nitrate salts were dissolved together in distilled water prior to the dropwise addition of diluted citric acid. The substituted perovskites containing K, Na, and Sr elements are labelled LKMO, LNMO, and LSMO, respectively.

## 2.2 Formaldehyde catalytic oxidation

HCHO catalytic oxidation was done in a fixed bed reactor with an internal diameter of 8 mm and a catalyst bed of 0.200 g, according to the procedure described elsewhere [4]. A constant concentration of 100 ppm of HCHO in a flow of 20 vol.% O<sub>2</sub> in He was generated using a permeation system (Dynacalibrator, VICI Metronics, Inc.), with the permeation tube filled with paraformaldehyde. All reactions were performed under the same mass-based space velocity of 30 L.g<sub>catal</sub><sup>-1</sup>.h<sup>-1</sup>. The outlet gas was monitored online using a gas chromatograph (Varian) equipped with a thermal conductivity detector. Separations were performed using two columns: one CP-Sil 5 CB column channel (8 m) for HCHO analysis, and one COX column channel (1 m) for CO<sub>2</sub> analysis.

HCHO conversion (equation 1) represents the oxidation of HCHO into CO<sub>2</sub>, while total removal of HCHO is given by HCHO elimination (equation 2). HCHO adsorption is deduced from the carbon balance (equation 3), knowing that no CO was detected when using GC-MS detection.

$$\text{HCHO conversion (into CO}_2\text{)} = \frac{[\text{CO}_2]_t}{[\text{HCHO}]_0} \quad (1)$$

$$\text{HCHO elimination} = \frac{[\text{HCHO}]_0 - [\text{HCHO}]_t}{[\text{HCHO}]_0} \quad (2)$$

$$\text{HCHO adsorption (\%)} = 100 - (\text{HCHO elimination} - \text{HCHO conversion}) \quad (3)$$

Where [HCHO]<sub>0</sub> is the initial HCHO concentration (100 ppm), and [HCHO]<sub>t</sub> and [CO<sub>2</sub>]<sub>t</sub> are their concentrations at a time *t*. Stability tests were carried on catalysts firstly activated 1h at 300 °C under a flow of 20 vol% O<sub>2</sub>/He (100 mL min<sup>-1</sup>). The temperature was then decreased to reach the temperature at which 50 % of the HCHO is converted (T<sub>50</sub>), and the reacting gas composed of 100 ppm HCHO in 20 vol% O<sub>2</sub>/He (100 mL min<sup>-1</sup>) went across the catalyst bed for at least 64 h.

Moreover, turnover frequencies (TOFs) were deduced from catalytic tests as follows [24]:

$$\text{TOF (s}^{-1}\text{)} = \frac{C_{\text{HCHO}}X_{\text{HCHO}}V_{\text{gas}}}{n_{\text{Mn}^{4+}}} \quad (4)$$

Where  $C_{\text{HCHO}}$  is the inlet HCHO concentration;  $X_{\text{HCHO}}$  is the HCHO conversion (into  $\text{CO}_2$ );  $V_{\text{gas}}$  is the total molar flow rate; and  $n_{\text{Mn}^{4+}}$  is the mole number of  $\text{Mn}^{4+}$  ions per gram of perovskite as estimated by  $\text{H}_2$ -TPR. While a contribution from  $\text{Mn}^{3+}$  species on the total catalytic activity cannot be ruled out completely, it remains negligible due to the much lower reducibility of Mn(III) compared to Mn(IV).

### 2.3 Characterization

Powder X-ray diffraction (PXRD) patterns were collected on a Bruker D8 Advanced AXS diffractometer. The diffractometer was operated at 40 kV and 30 mA and was equipped with a monochromatic radiation source ( $\lambda = 1.5418 \text{ \AA}$ ). Step time of 1 s and step size of  $0.02^\circ$  were used to record the X-ray diffractograms. Nitrogen sorption isotherms were measured at 77 K on a Micromeritics Flow Sorb III serial 416 apparatus. Prior to analysis, samples were degassed at 423 K during 6 h. The specific surface area ( $S_{\text{BET}}$ ) was determined according to the BET method, and the total pore volume ( $V_{\text{pore}}$ ) was estimated from the nitrogen adsorbed at  $P/P^0 = 0.99$ .

The Fourier transformed infrared (FTIR) spectra were recorded on a Thermo Scientific Nicolet iS50 FTIR spectrophotometer over the  $4000\text{-}400 \text{ cm}^{-1}$  range. High-resolution X-ray Photoelectron Spectra (XPS) were collected on a Kratos Analytical AXIS Ultra<sup>DLD</sup> spectrometer equipped with a monochromatic Al  $K\alpha$  X-ray source (1486.6 eV), with a constant pass energy of 20 eV. Spectral decomposition and quantification were done using CasaXPS, after calibration with adventitious C1s (284.8 eV).

CW-EPR experiments were performed using a Bruker ELEXYS E500 operating at 9.34 GHz. In situ EPR spectra were collected from room temperature until 580K with

a ramp of temperature of 10°/min. Microwave power was set to 1 mW and amplitude modulation to 4 G. The g factor is determined following the relation (5):

$$h\nu = g\beta B \quad (5)$$

Where h is the Planck's constant,  $\nu$  is the microwave frequency,  $\beta$  is the Bohr magneton constant, and B is the magnetic field.

Samples composition was evaluated using an Agilent Technologies 700 Series inductively coupled plasma-optical emission spectrometer (ICP-OES). The materials were dissolved in concentrated HCl/HNO<sub>3</sub> mixture prior to analysis. Temperature programmed reduction (TPR) profiles were acquired using a Micromeritics Autochem II 2920 apparatus. The materials were heated up to 1000 °C following a heating ramp of 10 °C.min<sup>-1</sup> under 5 vol% H<sub>2</sub>/Ar gas flow (50 mL.min<sup>-1</sup>). Oxygen temperature-programmed desorption (TPD) measurements were conducted after *in situ* activation at 40 °C under a flow of 5 vol% O<sub>2</sub>/He. Then, the solids were heated up to 1000 °C following a heating ramp of 10 °C/min under a gas flow of He (30 mL/min). A mass spectrometer allowed identification of O<sub>2</sub> (m/z = 32) in the outlet gases, and the amount of O<sub>2</sub> desorbed was quantified from calibrated pulses (1 μmol).

High angle annular dark field (HAADF) imaging and scanning transmission electron microscopy–energy dispersive X-ray spectroscopy (STEM-EDX) have been conducted using a FEG TEM/STEM system (Titan Themis FEI) operated at 300 kV. The microscope is equipped with a monochromator, a super-X windowless four-quadrant silicon drift detector (SDD) for the STEM-EDX mapping, and a probe Cs corrector allowing spatial resolution of about 65 pm. For both HAADF acquisitions and STEM-EDX mapping, the probe size was about 500 pm with screen currents comprised between 50 and 100 pA. Collection angles for the HAADF detector were comprised between 50 and 200 mrad. For the probe, a semi-convergence angle of 21 mrad was

used. Samples were directly observed as powders, and as thin foils. The thin foils (50 nm) were prepared using a Leica Ultracut S ultramicrotome, after dispersion of the samples within an epoxy resin and curing.

### 3 Results and Discussion

#### 3.1 PXRD and Nitrogen Physisorption

The PXRD patterns of all samples, displayed on Figure S1, match with the typical diffraction pattern of rhombohedral  $\text{LaMnO}_{3.15}$  (JCPDS 50-0298). No diffraction peak corresponding to a secondary crystalline phase, such as  $\text{La}_2\text{O}_3$  and  $\text{MnO}_x$ , can be observed. The average crystallite size ( $d_{\text{LMO}}$ ), determined when applying the Sherrer equation to the (024) plane, is about 19 to 25 nm (Table S1). Evidence of cations insertion within the perovskite structure can be deduced from the PXRD patterns (Figure S1, insert). When  $\text{La}^{3+}$  was substituted by  $\text{Na}^+$ , presenting a smaller ionic radius (1.22 Å against 1.06 Å, respectively), diffraction peaks are shifted toward smaller interreticular distances, while ions with larger radius (1.45 Å for  $\text{K}^+$ ) shifted the diffraction peaks toward larger interreticular distances [5]. As a direct consequence of inserting cations of different ionic radii, the lattice volume is modified and lattice distortions arise. On the other hand, when  $\text{La}^{3+}$  was substituted with  $\text{Sr}^{2+}$ , presenting a comparable ionic radius (1.23 Å), no shift can be observed.

$\text{N}_2$ -physisorption isotherms are presented on Figure S2, and the related textural data are given in Table S1. Isotherms are of Type 2 according to the IUPAC classification, which are characteristic of poorly porous solids. The notable  $\text{N}_2$  uptake above  $P/P^0 = 0.8$  fits with the formation of intercrystalline mesopores as well as small macropores due to the decomposition of the citrate precursor. As expected, all samples display relatively low specific surface areas (from 18 to 23  $\text{m}^2\cdot\text{g}^{-1}$ ) as well as limited pore volumes (from 0.06 to 0.10  $\text{cm}^3\cdot\text{g}^{-1}$ ). All these characteristics are related to the

high bulk density of the perovskite phase combined to the ~20 nm crystals size.

### 3.2 Elemental analysis

Chemical states and surface element compositions were evaluated by X-ray photoemission spectroscopy (XPS), while the bulk composition was determined by inductively coupled plasma analysis (ICP). All elemental data, including the molar ratio of adsorbed oxygen species, are summarized on Table 1. Moreover, EPR spectroscopy was conducted to probe the chemical environment of  $\text{Mn}^{4+}$  species.

Within experimental and apparatus errors, the determined atomic ratios of A/Mn by ICP are in close agreement with the nominal values except in the case of LNMO, possibly characterizing the presence of extra-lattice  $\text{Na}^+$ . LMO perovskite particles are known to present A-site enrichment at their surface [4], leading to La/Mn atomic ratios higher than 1 as obtained by XPS. By comparing ICP and XPS results for LKMO and LNMO, it seems clear that some extra-lattice  $\text{Na}^+$  are remaining in the case of LNMO, leading to its surface enrichment.

The La 3d, Sr 3d, Na 1s, K 2p, and Mn 2p XPS spectra for all samples are shown in Figure S3. Notably, Mn 2p region exhibits two photopeaks at ~642 eV and ~653 eV, which are respectively assigned to Mn 2p<sub>3/2</sub> and Mn 2p<sub>1/2</sub>. The Mn 3s region can be observed in Figure 1a. Owing to Mn 3s splitting value ( $\Delta E_s$ ), the average oxidation state (AOS) of surface Mn can be estimated from following the correlation:  $\text{AOS (Mn)} = 8.956 - 1.126 \times \Delta E_s$  [25]. In the case of LMO, the surface AOS (Mn) is 3.4 (Table 1), slightly higher than the theoretical value (3.3) and corresponding to a mixture of  $\text{Mn}^{4+}/\text{Mn}^{3+}$  with  $\text{Mn}^{3+}$  as the predominant cation. The Sr-, Na- and K- substituted samples (LSMO, LNMO and LKMO) show AOS (Mn) values of 3.5, 3.6 and 3.6 respectively. Despite the considerable margin of error (10%) on these values, it seems that  $\text{Mn}^{4+}$  enrichment occurs as a result of  $\text{La}^{3+}$  substitution by lower valency cations

(e.g.  $\text{Sr}^{2+}$ ,  $\text{Na}^+$ ,  $\text{K}^+$ ). However, according to the principle of electronic neutrality, the total charge of the lattice has to be balanced either by increasing the average oxidation state of the B-site cation or by the formation of oxygen vacancies ( $V_{\text{O}}$ ). Figure 1b displays high-resolution XPS spectra in the O1s region for all samples. Three components can be positioned at 529.3, 531.1, and 532.9 eV, attributed to the surface adsorbed oxygen species ( $\text{O}_2^-$ ,  $\text{O}_2^{2-}$  and  $\text{O}^-$ , labelled  $\text{O}_{\text{ads}}$ ), the surface lattice oxygens ( $\text{O}^{2-}$ , labelled  $\text{O}_{\text{latt}}$ ), and some adsorbed oxygen-containing groups including water and carbonate species (labelled  $\text{O}_{\text{w}}$ ), respectively [26]. Surface adsorbed oxygen species ( $\text{O}_{\text{ads}}$ ) are usually linked to surface oxygen vacancies [27], the latter providing sites for adsorption during the oxidation process:  $\text{O}_{2(\text{g})}$  will adsorb and dissociate on Mn(III) surface site, leading to the reoxydation of manganese to +IV. Consequently, the density of surface adsorbed oxygen species directly affect the oxidation performance [16].

Interestingly, all A-site substituted samples present significantly higher  $\text{O}_{\text{ads}}/\text{O}_{\text{tot}}$  (total amount of oxygen species, denoted  $\text{O}_{\text{tot}}$ ) ratio compared to the reference LMO ( $\text{O}_{\text{ads}}/\text{O}_{\text{tot}} = 0.43\text{-}0.46$  vs. 0.34, Table 1). Supposing constant surface oxygen-containing groups ( $\text{O}_{\text{w}}$ ), this increase could be ascribed to a higher concentration of surface adsorbed oxygen species. It should be noted that the binding energy of  $\text{O}_{\text{latt}}$  is shifted to lower values in the case of LNMO and LKMO (Figure 1b). This evolution could be related to the notable difference in ionic radii between  $\text{Na}^+/\text{K}^+$  and  $\text{La}^{3+}$ , inducing deformations in the crystal network and weakening Mn-O bonds [19]. The latter would enhance lattice oxygen mobility.

Oxygen vacancies, which are often postulated in oxidation mechanisms, were probed by EPR spectroscopy. EPR spectra of as-made LMO and LNMO are represented on Figure 2. For LMO, the presence of Mn(IV) species is clearly reflected by the signal centred at  $g = 1.96$ . Interestingly, this signal is shifted toward a  $g$  factor of 1.99 for

LNMO, indicating a different chemical environment around Mn(IV) and supporting the successful insertion of Na<sup>+</sup> within the perovskite framework as well as possible distortions of the crystal lattice. Importantly, no sharp signal between  $g = 1.96$  (shallow donor) and 2.01 (acceptor vacancies) was detected in any spectrum [28]. Therefore, these results contradict the presence of consequent oxygen vacancies in the materials, and pledge for an increase of the average oxidation state of Mn species.

### 3.3 Reducibility and oxygen reactivity studies

H<sub>2</sub>-TPR profiles and related data are shown in Figure 3 and in Table 2, respectively. LMO presents one major peak centered at 377 °C, assigned to the reduction of Mn<sup>4+</sup> into Mn<sup>3+</sup>, and a shoulder around 470 °C, associated to the partial reduction of Mn<sup>3+</sup> into Mn<sup>2+</sup> [7]. Over 600 °C, the intense peak refers to the reduction of the remaining Mn<sup>3+</sup> to Mn<sup>2+</sup>. A close fit is observed between the theoretical (2.70 mmol/g) and experimental (2.66 mmol/g) values of H<sub>2</sub> consumption.

The main peak for Sr- and K-substituted samples LSMO and LKMO is shifted to lower temperatures (365 °C and 360 °C, respectively), while a lower temperature shoulder (349 °C) appears for LNMO, indicating facilitated reduction of Mn<sup>4+</sup>. Also, the onset temperature ( $T_{\text{onset}}$ ) is below 150 °C for all A-site substituted perovskites, about 100 °C lower than the reference LMO. This initial hydrogen consumption is attributed to the elimination of surface oxygen adsorbed species (adspecies). The total H<sub>2</sub> consumption at low temperature (< 600 °C) was 1.58, 1.63 and 1.67 mmol/g for samples LSMO, LNMO and LKMO, respectively, while 1.37 mmol/g of H<sub>2</sub> was consumed in the same temperature range by the reference LMO. This is in line with the increase of Mn(IV) species as seen by EPR and XPS.

As determined on Figure S4 the initial H<sub>2</sub> consumption rate, and therefore the low temperature reducibility [29], decreases in the following order: LSMO > LKMO ≈

LNMO > LMO. When the temperature is increased, the reducibility of the alkali-substituted samples increases faster. These results indicate that the partial substitution of  $\text{La}^{3+}$  cations by  $\text{Sr}^{2+}$ ,  $\text{Na}^+$  or  $\text{K}^+$  promotes low temperature reducibility of LMO-based catalysts, in addition to an increased concentration of adspecies, which should have a beneficial effect for oxidation reactions.

$\text{O}_2$ -TPD profiles were used to estimate both the surface and bulk oxygens reactivity. The related MS signals ( $m/z = 32$ ) are presented on Figure 4. LMO only presents one main oxygen loss observed above  $750\text{ }^\circ\text{C}$  (region III), referring to the release of lattice oxygen from the bulk ( $\text{O}_{\text{lat}}$ ). Additionally, a weak desorption is observed between  $300$  and  $440\text{ }^\circ\text{C}$  ( $\alpha\text{-O}_2$ ). Therefore, LMO is expected to perform poorly for low temperature oxidation.

A-site substituted samples present, on the other hand, two desorption domains at low temperature (region I at  $T = 100\text{-}440\text{ }^\circ\text{C}$  and region II at  $T = 440\text{-}750\text{ }^\circ\text{C}$ ), related to  $\alpha$  and  $\beta$  oxygen species, respectively [30,31]. The first peak below  $440\text{ }^\circ\text{C}$  (region I) is ascribed to the release of the weakly adsorbed surface oxygen species (e.g.  $\text{O}^-$  and  $\text{O}_2^-$ ), as well as some oxygen species from the subsurface lattice ( $\text{O}^{2-}$ ). The second peak below  $750\text{ }^\circ\text{C}$  (region II) can be attributed to the reduction of bulk Mn(IV) species by the outward diffusion of oxygen species ( $\text{O}^{2-}$ ). Thus the A-site substituted perovskites (LSMO, LNMO and LKMO) possess more surface active oxygen species. Moreover, the results suggest that oxygen mobility from the bulk is strongly improved for these samples.

### 3.4 Catalytic activity

HCHO catalytic oxidation in the presence of the different perovskite-based materials is presented on Figure 5 and in Table 3. Lower reaction temperatures are obtained in the presence of the A-site substituted catalysts, compared to the reference

LMO. Especially, LKMO achieves a remarkably low  $T_{50}$  (corresponding to the temperature at which 50% of the initial HCHO is converted) of 108 °C, substantially lower than LNMO (123 °C), LSMO (133 °C) and LMO (145 °C).

Alkali ions have been reported to favor adsorption of HCHO over catalysts [15-17]. Therefore, this parameter should be taken into account, both to better understand the HCHO oxidation mechanism, and to discriminate adsorption from catalytic oxidation. From the results, A-site substitution by alkali ions clearly promotes the total HCHO elimination at low temperature following adsorption, as illustrated by the carbon balance. Moreover, the onset temperature ( $T_{\text{onset}}$ ) in the presence of LNMO or LKMO is as low as room temperature, while it increases to 68 °C and 112 °C in the presence of LSMO and LMO, respectively.

To brush off the potential influence of the surface area, which is proportional to the number and accessibility of active and/or adsorption sites, on the conversion rate, the corresponding specific HCHO reaction rate ( $R_s$ ) at 110 °C was calculated. As displayed in Table S1, LKMO showed the highest specific HCHO reaction rate ( $0.79 \mu\text{mol s}^{-1} \text{m}^{-2}$ ) - seven times higher than LMO ( $0.12 \mu\text{mol s}^{-1} \text{m}^{-2}$ ) - followed by LNMO ( $0.45 \mu\text{mol s}^{-1} \text{m}^{-2}$ ) and LSMO ( $0.32 \mu\text{mol s}^{-1} \text{m}^{-2}$ ).

The Arrhenius plots corresponding to each material are presented on Figure S5.a, and the related apparent activation energy ( $E_a$ ) are indicated in Table S1. The  $E_a$  values of Na- and K-substituted perovskites are 46.5 and 63.5 kJ/mol respectively, which are within the range of supported noble metal catalysts (Table S2), confirming their high potential as catalysts. Moreover, the turnover frequencies (TOFs) were determined for all perovskite-based catalysts and presented in Figure S5.b. At 100 °C, their respective TOFs values are  $0.49 \cdot 10^{-3} \text{ s}^{-1}$ ,  $1.35 \cdot 10^{-3} \text{ s}^{-1}$ ,  $2.63 \cdot 10^{-3} \text{ s}^{-1}$  and  $2.74 \cdot 10^{-3} \text{ s}^{-1}$ . For comparison, TOFs values from 3-dimensional transition metal oxides ( $\text{MnO}_2$  and

Co<sub>3</sub>O<sub>4</sub>) and supported silver catalysts, which have been highlighted as efficient catalysts for HCHO oxidation, are also indicated on Figure S5 as well as in Table S2. As expected, supported noble metal-based catalysts exhibit higher TOF values for the same reaction temperature, however they remain in the same range as the alkali ion-substituted perovskites LNMO and LKMO. Moreover, LNMO and LKMO are more active for HCHO oxidation than other reported transition metal-based catalysts.

Briefly, LKMO and LNMO present relatively high specific reaction rates and TOFs, implying that they are attractive catalysts for low temperature HCHO oxidation. Their improved catalytic activity might stem from two main factors. Firstly, the substituted perovskites present enhanced low-temperature adsorption capacity of HCHO (see Fig. 5) owing to their high concentration of surface adsorbed oxygen species. Indeed, surface oxygen species including hydroxyl groups can directly react with HCHO to form formate and carbonate species [32]. Secondly, the performance of a catalyst in oxidation is typically related to its oxidizing capacity, which has been demonstrated as superior in the case of all A-site substituted LMO perovskites. Not only Mn<sup>4+</sup> enrichment enhances the catalytic action of the redox cycle by supplying active oxygen species during the reaction [27,33], but it also favours surface adsorption site formation [16]. By participating to the adsorption of dioxygen molecules, their further dissociation into active oxygen species, and their inner migration [34], surface adsorption sites have a major contribution to the global catalytic mechanism. Thus, HCHO catalytic oxidation may be considered dependant of the surface properties, and the reactivity of Mn<sup>4+</sup>/Mn<sup>3+</sup> redox cycle.

### *3.5 Effect of alkali ion substitution on HCHO oxidation mechanism*

The formation of intermediate species on the catalysts surface was probed using ATR-FTIR, before and after HCHO exposure (Figure S6). Over LMO before HCHO

exposure, two main bands at  $1382\text{ cm}^{-1}$  and  $1476\text{ cm}^{-1}$  are observed, belonging to the C-O stretching of carbonate species usually found after the preparation of La-based perovskites [35]. The three A-site substituted perovskites also exhibit similar bands, with an additional peak using LSMO around  $1445\text{ cm}^{-1}$  possibly corresponding to  $\text{SrCO}_3$  (Figure S7).

After HCHO oxidation, two new strong bands appear in all samples at  $1354$  and  $1575\text{ cm}^{-1}$ , assigned to formate species  $\nu_s(\text{COO})$  and  $\nu_{as}(\text{COO})$  respectively. Two other bands, around  $1386$  and  $2838\text{ cm}^{-1}$ , are also assigned to formate species (eg.,  $\delta(\text{CH})$  and  $\nu(\text{CH})$ ) [32,36]. Additionally, three bands of lower intensity can be observed on the spectra of the A-site substituted perovskites. One, around  $1428\text{ cm}^{-1}$  ( $\delta(\text{CH}_2)$ ), is attributed to dioxymethylene (DOM,  $\text{H}_2\text{CO}_2$ ) [37], which is a well-known intermediate that easily oxidize to formate ( $\text{HCOO}^-$ ) [19]. The two other bands, at  $1406$  and  $1497\text{ cm}^{-1}$ , belong to surface carbonate species (e.g.  $\text{CO}_3^{2-}$ ) [14,32]. In contrast, a very weak shoulder around  $1500\text{ cm}^{-1}$ , also attributed to  $\text{CO}_3^{2-}$  presence, is observed on the spent LMO. These observations underline the improved adsorption of dioxymethylene, formate and carbonate species on the surface of all A-site substituted perovskites. This is in line with the study of S. Selvakumar *et al.* on birnessite [38], who reported that formate species can interact both with Mn and K ions, while carbonate species interact only with K ions. This, in turn, also means that La interacts weakly with carbonate species.

Prior investigations reported that oxidation of HCHO first generates formate species, which are further oxidized into  $\text{CO}_2$  in the presence of surface oxygen species [32,36,38]. Two oxidation mechanisms are usually discussed. While not incompatible, they are likely to present different reaction kinetics and intermediates formation, depending on the degree of participation of surface -OH groups. They play a critical

role in HCHO oxidation at low temperature by enhancing HCHO adsorption *via* hydrogen bonding, while facilitating its activation [32]. When abundant surface -OH groups are present, direct oxidation of formate species ( $\text{HCOO}^-_{\text{ads}}$ ) into  $\text{CO}_2$  is preferred (route A). In contrast, when a catalyst lacks surface -OH groups, the formate species may tend to decompose into water and surface -CO, which is then oxidized into  $\text{CO}_2$  by the active oxygen (*e.g.*  $\text{O}_2^{2-}$ ,  $\text{O}_2^-$ ,  $\text{O}^-$ , *etc.* denoted by  $\text{O}^*$ ) species (route B). Based on XPS, ATR-FTIR, and  $\text{O}_2$ -TPD, the A-site substituted perovskites likely follow route A, while the reference LMO would rather follow route B.



$\text{O}_2$ -TPD, ATR-FTIR and XPS highlighted the positive effect of A-site substitution on surface oxygen species ( $\text{O}^-$ ,  $\text{O}_2^-$ , and potentially -OH) density and reactivity, but the role of bulk oxygen species ( $\text{O}^{2-}$ ) remains unclear. Thus, temperature-programmed oxidation of HCHO over pre-saturated LMO and LNMO were followed by EPR under inert conditions and the results are presented on Figure 6. First, the EPR integrated signal of LNMO at room temperature is higher than that of LMO, meaning that more  $\text{Mn}^{4+}$  species are initially present in LNMO. This is in line with XPS and  $\text{H}_2$ -TPR measurements. Interestingly, the results evidenced two different mechanisms depending on the material. In the case of LMO (Fig. 6.a), there is only a slight difference in terms of Mn(IV) content between the starting HCHO-saturated material, and the ending material which was gradually heated up to about 300 °C then cooled down back to room temperature. Therefore, the  $\text{O}^{2-}$  bulk oxygen species were not consumed. This further means that HCHO is likely to be oxidized over LMO by surface adsorbed oxygen species, leading to reduced surface Mn(III) sites replenished by dissociative adsorption of gaseous oxygen molecules for further reaction.

On the other hand, a drastic decrease of the EPR signal of Mn(IV) is observed below 350 K in the case of HCHO-saturated LNMO (Fig. 6.b). This observation can only be explained by a massive consumption of  $\text{O}^{2-}$  oxygen species from the material

bulk starting as soon as the temperature increases, leading to the reduction of Mn(IV) into Mn(III) (species which cannot be observed by EPR). Thus, in opposition to what was observed with the unsubstituted LMO perovskite, partial substitution of La<sup>3+</sup> by alkali ions allows O<sup>2-</sup> oxygen species to react below 350 K. In addition, the EPR spectra demonstrated that at least a small part of Mn(III) is further reduced into Mn(II) while no significant oxygen vacancies are formed. When the temperature returned to room temperature, EPR demonstrated that 84% of the Mn(IV) was consumed in total, and the position of the EPR spectra suggests that Mn(II) species are no more present. These results support a Mars and van Krevelen redox mechanism involving the participation of bulk O<sup>2-</sup> species during the HCHO oxidation reaction, despite the low reaction temperature, over LNMO.

Based on this discussion, a possible mechanism pathway for HCHO oxidation by A-site substituted perovskites is proposed on Figure S8.

### *3.6 Stability test and effect of humidity*

Figure S9 displays HCHO elimination and conversion over time under dry stream at T<sub>50</sub> over LSMO, LNMO, LKMO and LMO. Over the first hours, HCHO conversion increases over the three A-site substituted perovskites, which might be due to reaction between adsorbed HCHO with adsorbed oxygen species [39]. However, a substantial decrease of both HCHO conversion (Fig. S9.a) and HCHO elimination (Fig. S9.b) is observed overtime with the substituted perovskites, while LMO activity remains relatively stable.

To better understand the undergoing phenomena, the spent catalysts were characterized by PXRD, XPS, TPR and TEM. The PXRD patterns (Figure S10) of the spent catalysts do not change significantly over the course of the reaction, meaning that no major phase transition nor collapsing occur. High resolution HAADF images of the spent LNMO catalyst are given on Figure 7. The upper-right HAADF image is a magnification of the green area marked on Figure 7.a. Those images are coherent with a LMO perovskite grain seen in the (130) crystallographic plane. For this

crystallographic projection the observable interplanar distances of 3.81 Å, 1.75 Å and 1.62 Å correspond, within experimental errors, to the respective crystallographic distances of the (002), (310) and (312) planes of the perovskite lattice. This is in agreement with PXRD, confirming that no significant structural changes have occurred. Figures 7.c to 7.f display STEM-EDX elemental mapping of La (green), Mn (red), Na (light blue) and O (dark blue). Na remains homogeneously distributed at the nanometric scale after HCHO oxidation. The average relative elemental quantification, (La: 18 at%, Na: 2 at%, Mn: 18 at%, O: 63 at%) is in agreement, within experimental and quantification procedure errors, with the composition of the fresh LNMO catalyst. Homogeneous distribution of Na cations over the grain is clearly visible (Fig. S7.e).

The intensity of the HAADF signal depends on the thickness, density and atomic number as approximately  $Z^{1.7}$  [40]. This means that heavier elements will appear with brighter intensities on HAADF images. Therefore, on Figure 7.b the brightest columns correspond to atomic La arrays (green arrow), while adjacent darker columns (red arrow) correspond to atomic Mn arrays. A closer look at the La arrays reveals the presence of atoms with lower contrast (black arrows), which could correspond to inserted Na. Thus, Na ions remain homogeneously distributed and well integrated in the perovskite crystal lattice at the atomic level even after the catalytic test.

However, as displayed on Figure S11.a, an appreciable change of XPS spectra in the Mn 3s region is observed compared to the fresh catalysts. After HCHO oxidation, the surface average oxidation state of Mn decreased from 3.51 to 3.10, 3.55 to 2.68, 3.63 to 2.99 and 3.40 to 3.26 over LSMO, LNMO, LKMO and LMO, respectively. The substitution of  $\text{La}^{3+}$  by elements of lower valence thus accelerates the reduction of lattice  $\text{Mn}^{4+}$  into  $\text{Mn}^{3+/2+}$  through bulk oxygen mobility, as observed by *in situ* EPR.

Similarly, at the low temperature region (200-650 °C) of the TPR profile (Figure

S11.b), the amount of consumed  $H_2$  is lower for all spent samples (LSMO: 0.83 mmol/g; LMO: 1.12 mmol/g) compared to the fresh catalysts (LSMO: 1.58 mmol/g; LMO: 1.37 mmol/g), correlating the XPS results. Additionally, the  $H_2$ -TPR profile of all spent catalysts are shifted to higher temperatures, suggesting lower reducibilities. Remarkably, in the case of alkali-substituted perovskites (LNMO and LKMO), two negative peaks around 320 °C are underlined by the dotted area in Figure 9b. This peak could belong to the desorption of HCHO intermediates, such as formate and carbonate species, which were firmly adsorbed on the used catalysts surface.

XPS spectra in the O1s region of the catalysts before and after reaction are superimposed on Figure S12. After reaction, the intensity of bulk oxygen species ( $O_{latt}$ ) decreases considerably with LNMO (Fig. S12.b) and LKMO (Fig. S12.c), while it decreases only slightly with LSMO (Fig. S12.a). This correlates with the observed global manganese reduction. Also, a new intense band noted  $O_F$  appears at high binding energy (531.5 eV) for LSMO, LNMO and LKMO. This new band is associated to O=C and O-C groups from adsorbed formaldehyde and formate species [38]. Their presence is also attested by XPS spectroscopy in the C1s region (Fig. S13), through a new component noted  $C_F$  and emerging around 288.6 eV [38,41]. EPR spectroscopy (Fig. S14) conducted on the spent LNMO further underlines the total reduction of Mn(IV) species into Mn(III) and Mn(II). In contrast, no significant difference is observed with the spent LMO, which is probably due to the higher reaction temperature used ( $T_{50}$ ). The latter should favor the  $O_{latt}$  reincorporation rate as well as the desorption of adspecies (Fig. S12.d and S13.d).

During the HCHO oxidation process, HCHO is first adsorbed on the catalyst surface, and then oxidized by surface active oxygen species into DOM, formate, carbonate and finally to  $CO_2$ . Then the consumed surface oxygen species are

replenished *via* the adsorption and dissociation of dioxygen and/or water, or by the migration of bulk oxygen species. Thus, the catalytic mechanism is cyclic and involves transition metal valence shifts [42]. In the short term, the adsorption and accumulation of HCHO and relating intermediates on the catalyst surface allow to obtain higher conversions. However, in the long term, a large accumulation of these species on the surface will not only result in a drastic consumption of surface active oxygen species and Mn(IV) species, but it also prevents the transfer of oxygen from gas-phase to  $O_{\text{latt}}$  through the adsorption-dissociation-incorporation mechanism [20,43]. Thus, the HCHO oxidation activity of the A-site substituted perovskites is rapidly inhibited, due to the decrease of lattice oxygens content, reservoir of reactive oxygen species.

According to the literature [14,15], the doping of noble metal-supported catalysts by alkali ions including  $\text{Na}^+$  and  $\text{K}^+$  has a drastic promotion effect on HCHO oxidation, however their tests are usually conducted under controlled humidity. In fact, water presence is considered as a major parameter for HCHO catalytic abatement [4,43]. High relative humidity has been reported to provoke a notable loss of HCHO oxidation activity due to competitive adsorption on the active sites [33]. Meanwhile, another study reported that water presence not only favours the desorption of carbonate species, but it also helps regenerating the hydroxyl groups [32,44]. Thus it is essential to investigate whether a controlled humidity can improve the long-term performances of the alkali-substituted perovskites (LNMO and LKMO).

The fresh catalysts were tested again in the presence of a humid gas stream (RH = 46%) at  $T_{50}$ , as shown on Figure 8. Compared to the stability results in dry conditions (Fig. S9), the presence of  $\text{H}_2\text{O}$  greatly improves the overtime catalytic activity of LNMO and LKMO, with only a small overtime reduction of HCHO conversion and HCHO elimination. In addition, the K-substituted perovskite presents a more durable

activity than the Na-substituted perovskite. Thus in our conditions and as reported in the case of birnessite [32], water is expected to avoid an accumulation of formate and carbonate species at the catalysts surface, as well as to regenerate the surface hydroxyl groups. Moreover, activation of H<sub>2</sub>O is expected to be facilitated by the presence of alkali elements within the perovskite framework [14]. This is supported by EPR spectroscopy conducted on spent LNMO, showing comparable content of Mn(IV) species with the fresh LNMO catalyst (Fig. S12).

#### 4. Conclusions

This study presented the preparation of A-site alkali- (Na<sup>+</sup>, K<sup>+</sup>) and alkaline earth-substituted (Sr<sup>2+</sup>) La<sub>1-x</sub>A<sub>x</sub>MnO<sub>3</sub> perovskites, their extensive characterization and their application to formaldehyde oxidation. All substituted perovskites presented higher HCHO oxidation activity than the reference LMO. Especially, a T<sub>50</sub> of 108 °C was obtained with LKMO, which is the lowest T<sub>50</sub> temperature reported so far with perovskites. Those improved catalytic performances stem from a larger amount of active oxygen species as well as the participation of bulk oxygen in the oxidation mechanism due to the higher reactivity of Mn<sup>4+</sup> species located in the bulk of the substituted materials.

Stability tests in dry and humid conditions were conducted over 65 h on LMO and the three A-site substituted perovskites. While the substituted perovskites initially presented higher catalytic activity, a fast deactivation was observed during reaction under dry conditions. This deactivation was attributed to the presence of abundant adsorbed oxidation intermediates (dioxymethylene, carbonate, formate), inhibiting the replenishment of surface oxygen species by molecular oxygen, and overtime depletion of bulk oxygen species. Interestingly, deactivation was minimized when humidity was added to the carrier gas, allowing the catalysts to present long-term activity. In brief,

these results shed light on the catalytic promoting effect of alkali-substituted perovskites, which shall guide future research toward the further improvement of perovskite-based catalysts for the development of low-cost, high-efficiency materials for indoor pollution control.

### **CRedit author statement**

**Yin Xu:** investigation, formal analysis, data curation, writing – original draft preparation. **Jérémy Dhainaut:** writing – review & editing, supervision. **Jean-Philippe Dacquin:** supervision. **Anne-Sophie Mamede:** formal analysis, investigation. **Maya Marinova:** formal analysis, investigation. **Jean-François Lamonier:** supervision. **Hui Zhang:** supervision, funding acquisition. **Sébastien Royer:** supervision, funding acquisition.

### **Declaration of interests**

The authors declare that they have no known competing financial interests or personal relationships that could have appeared to influence the work reported in this paper.

## Acknowledgments

The CNRS, the Chevreul Institute (FR 2638), the Ministère de l'Enseignement Supérieur et de la Recherche, the Région Hauts-de-France and the FEDER are acknowledged for supporting this work. Yin Xu acknowledges the China Scholarship Council (No. 201606270079) for the financial support for the PhD program. The authors acknowledge Dr. Pardis Simon (UCCS) for XPS characterizations.

## References

- [1] Murray, C.J.L. *et coll.* Global, regional, and national comparative risk assessment of 84 behavioral, environmental and occupational, and metabolic risks or clusters of risks for 195 countries and territories, 1990-2017: a systematic analysis for the GBD Study 2017. *Lancet* 2018, 392, 1923-1994.
- [2] Huang, Q.; Hu, Y.; Pei, Y.; Zhang, J.; Fu, M. In situ synthesis of TiO<sub>2</sub>@NH<sub>2</sub>-MIL-125 composites for use in combined adsorption and photocatalytic degradation of formaldehyde. *Appl. Catal. B* 2019, 259, 118106.
- [3] Guo, J.; Lin, C.; Jiang, C.; Zhang, P. Review on noble metal-based catalysts for formaldehyde oxidation at room temperature. *Appl. Surf. Sci.*, 2019, 475, 237-255.
- [4] Xu, Y.; Dhainaut, J.; Rochard, G.; Dacquin, J.-P.; Mamede, A.-S.; Giraudon, J.-M.; Lamonier, J.-F.; Zhang, H.; Royer, S. Hierarchical porous  $\epsilon$ -MnO<sub>2</sub> from perovskite precursor: Application to the formaldehyde total oxidation. *Chem. Eng. J.*, 2020, 388, 124146.
- [5] Royer, S.; Duprez, D.; Can, F.; Courtois, X.; Batiot-Dupeyrat, C.; Laassiri, S.; Alamdari, H. Perovskites as substitutes of noble metals for heterogeneous catalysis: dream or reality, *Chem. Rev.* 2014, 114, 10292-10368.
- [6] Hwang, J.; Rao, R.R.; Giordano, L.; Katayama, Y.; Yu, Y.; Shao-Horn, Y.

- Perovskites in catalysis and electrocatalysis, *Science* 2017, 358, 751-756.
- [7] Royer, S.; Alamdari, H.; Duprez, D.; Kaliaguine, S. Oxygen storage capacity of  $\text{La}_{1-x}\text{A}'_x\text{BO}_3$  perovskites (with  $\text{A}' = \text{Sr}, \text{Ce}$ ;  $\text{B} = \text{Co}, \text{Mn}$ )-relation with catalytic activity in the  $\text{CH}_4$  oxidation reaction. *Appl. Catal. B* 2005, 58, 273-288.
- [8] Royer, S.; Levasseur, B.; Alamdari, H.; Barbier Jr, J.; Duprez, D.; Kaliaguine, S. Mechanism of stearic acid oxidation over nanocrystalline  $\text{La}_{1-x}\text{A}'_x\text{BO}_3$  ( $\text{A}' = \text{Sr}, \text{Ce}$ ;  $\text{B} = \text{Co}, \text{Mn}$ ): The role of oxygen mobility. *Appl. Catal. B* 2008, 80, 51-61.
- [9] Onrubia-Calvo, J.A.; Pereda-Ayo, B.; De-La-Torre, U.; González-Velasco, J.R. Key factors in Sr-doped  $\text{LaBO}_3$  ( $\text{B} = \text{Co}$  or  $\text{Mn}$ ) perovskites for NO oxidation in efficient diesel exhaust purification. *Appl. Catal. B* 2017, 213, 198-210.
- [10] Ji, Q.; Bi, L.; Zhang, J.; Cao, H.; Zhao, X.S. The role of oxygen vacancies of  $\text{ABO}_3$  perovskite oxides in the oxygen reduction reaction. *Energ. Environ. Sci.* 2020, 13, 1408-1428.
- [11] Marakatti, V. S.; Gaigneaux, E.M. Recent advances in heterogeneous catalysis for ammonia synthesis. *ChemCatChem* 2020, 12, 5838-5857.
- [12] Li, Z.; Zhong, L.; Yu, F.; An, Y.; Dai, Y.; Yang, Y.; Lin, T.; Li, S.; Wang, H.; Gao, P.; Sun Y.; He, M. Effects of sodium on the catalytic performance of CoMn catalysts for Fischer-Tropsch to olefin reactions. *ACS Catal.* 2017, 7, 3622-3631.
- [13] Wei, J.; Ge, Q.; Yao, R.; Wen, Z.; Fang, C.; Guo, L.; Xu, H.; Sun, J. Directly converting  $\text{CO}_2$  into a gasoline fuel. *Nat. Commun.* 2017, 8, 15174.
- [14] Zhang, C.; Liu, F.; Zhai, Y.; Ariga, H.; Yi, N.; Liu, Y.; Asakura, K.; Flytzani-Stephanopoulos, M.; He, H. Alkali-metal-promoted  $\text{Pt}/\text{TiO}_2$  opens a more efficient pathway to formaldehyde oxidation at ambient temperatures. *Angew. Chem. Int. Ed.* 2012, 51, 9628-9632.

- [15] Zhang, C.; Li, Y.; Wang, Y.; He, H. Sodium-promoted Pd/TiO<sub>2</sub> for catalytic oxidation of formaldehyde at ambient temperature. *Environ. Sci. Technol.* 2014, 48, 5816-5822.
- [16] Bai, B.; Li, J. Positive effects of K<sup>+</sup> ions on three-dimensional mesoporous Ag/Co<sub>3</sub>O<sub>4</sub> catalyst for HCHO oxidation. *ACS Catal.* 2014, 4, 2753-2762.
- [17] Nie, L.; Yu, J.; Li, X.; Cheng, B.; Liu, G.; Jaroniec, M. Enhanced performance of NaOH-modified Pt/TiO<sub>2</sub> toward room temperature selective oxidation of formaldehyde. *Environ. Sci. Technol.* 2013, 47, 2777-2783.
- [18] Ji, J.; Lu, X.; Chen, C.; He, M.; Huang, H. Potassium-modulated δ-MnO<sub>2</sub> as robust catalysts for formaldehyde oxidation at room temperature. *Appl. Catal. B* 2020, 260, 118210.
- [19] Rong, S.; Li, K.; Zhang, P.; Liu, F.; Zhang, J. Potassium associated manganese vacancy in birnessite-type manganese dioxide for airborne formaldehyde oxidation. *Catal. Sci. Technol.* 2018, 8, 1799-1812.
- [20] Wang, J.; Li, J.; Zhang, P.; Zhang, G. Understanding the “seesaw effect” of interlayered K<sup>+</sup> with different structure in manganese oxides for the enhanced formaldehyde oxidation. *Appl. Catal. B* 2018, 224, 863-870.
- [21] Lee, Y.N.; Lago, R.M.; Fierro, J.L.G.; Cortes, V.; Sapiña, F., Martinez, E. Surface properties and catalytic performance for ethane combustion of La<sub>1-x</sub>K<sub>x</sub>MnO<sub>3+δ</sub> perovskites. *Appl. Catal. A* 2001, 207, 17-24.
- [22] Hong, W.; Zhen, Z.; Xu, C.-M.; Jian, L. Nanometric La<sub>1-x</sub>K<sub>x</sub>MnO<sub>3</sub> perovskite-type oxides – highly active catalysts for the combustion of diesel soot particle under loose contact conditions. *Catal. Letters*, 2005, 102, 251-256.
- [23] Buciuman, F.-C.; Patcas, F.; Menezes, J.-C.; Barbier, J.; Hahn, T.; Lintz, H.-G. Catalytic properties of La<sub>0.8</sub>A<sub>0.2</sub>MnO<sub>3</sub> (A = Sr, Ba, K, Cs) and LaMn<sub>0.8</sub>B<sub>0.2</sub>O<sub>3</sub> (B =

- Ni, Zn, Cu) perovskites: 1. Oxidation of hydrogen and propene. *Appl. Catal. B* 2002, 35, 175-183.
- [24] Bai, B.; Qiao, Q.; Arandiyán, H.; Li, J.; Hao, J.; Three-dimensional ordered mesoporous MnO<sub>2</sub>-supported Ag nanoparticles for catalytic removal of formaldehyde. *Environ. Sci. Technol.* 2016, 50, 2635-2640.
- [25] Yang, Y.; Huang, J.; Wang, S.; Deng, S.; Wang, B.; Yu, G. Catalytic removal of gaseous unintentional POPs on manganese oxide octahedral molecular sieves. *Appl. Catal., B* 2013, 142-143, 568-578.
- [26] Santos, V.P.; Pereira, M.F.R.; Órfão, J.J.M.; Figueiredo, J.L. The role of lattice oxygen on the activity of manganese oxides towards the oxidation of volatile organic compounds. *Appl. Catal. B* 2010, 99, 353-363.
- [27] Ye, J.; Zhou, M.; Le, Y.; Cheng, B.; Yu, J. Three-dimensional carbon foam supported MnO<sub>2</sub>/Pt for rapid capture and catalytic oxidation of formaldehyde at room temperature. *Appl. Catal. B* 2020, 267, 118689.
- [28] Drouilly, C.; Krafft, J.-M.; Averseng, F.; Casale, S.; Bazer-Bachi, D.; Chizallet, C.; Lecocq, V.; Vezin, H.; Lauron-Pernot, H.; Costentin, G. ZnO Oxygen Vacancies Formation and Filling Followed by in Situ Photoluminescence and in Situ EPR. *J. Phys. Chem. C*, 2012, 116, 21297-21307.
- [29] Wang, F.; Dai, H.; Deng, J.; Bai, G.; Ji, K.; Liu, Y. Manganese oxides with rod-, wire-, tube-, and flower-like morphologies: highly effective catalysts for the removal of toluene. *Environ. Sci. Technol.* 2012, 46, 4034-4041.
- [30] Zhang, C.; Wang, C.; Zhan, W.; Guo, Y.; Guo, Y.; Lu, G.; Baylet, A.; Giroir-Fendler, A. Catalytic oxidation of vinyl chloride emission over LaMnO<sub>3</sub> and LaB<sub>0.2</sub>Mn<sub>0.8</sub>O<sub>3</sub> (B= Co, Ni, Fe) catalysts. *Appl. Catal. B* 2013, 129, 509-516.
- [31] Zhang, C.; Wang, C.; Gil, S.; Boreave, A.; Retailleau, L.; Guo, Y.; Valverde, J.L.; Giroir-Fendler, A. Catalytic oxidation of 1,2-dichloropropane over supported

- LaMnO<sub>x</sub> oxides catalysts. *Appl. Catal. B* 2017, 201, 552-560.
- [32] Wang, J.; Zhang, P.; Li, J.; Jiang, C.; Yunus, R.; Kim, J. Room-temperature oxidation of formaldehyde by layered manganese oxide: effect of water. *Environ. Sci. Technol.* 2015, 49, 12372-12379.
- [33] Tang, X.; Li, Y.; Huang, X.; Xu, Y.; Zhu, H.; Wang, J.; Shen, W. MnO<sub>x</sub>-CeO<sub>2</sub> mixed oxide catalysts for complete oxidation of formaldehyde: effect of preparation method and calcination temperature. *Appl. Catal. B* 2006, 62, 265-273.
- [34] Wang, Y., Liu, K., Wu, J., Hu, Z., Huang, L., Zhou, J., Ishihara, T., Guo, L. Unveiling the effects of alkali metal ions intercalated in layered MnO<sub>2</sub> for formaldehyde catalytic oxidation. *ACS Catal.* 2020, 10, 10021-10031.
- [35] Dacquin, J.-P.; Lancelot, C.; Dujardin, C.; Cordier-Robert, C.; Granger, P. Support-induced effects of LaFeO<sub>3</sub> perovskite on the catalytic performances of supported Pt catalysts in DeNO<sub>x</sub> applications. *J. Phys. Chem. C* 2011, 115, 1911-1921.
- [36] Quiroz, J.; Giraudon, J.-M.; Gervasini, A.; Dujardin, C.; Lancelot, C.; Trentesaux, M.; Lamonier, J.-F. Total oxidation of formaldehyde over MnO<sub>x</sub>-CeO<sub>2</sub> catalysts: The effect of acid treatment, *ACS Catal.* 2015, 5, 2260-2269.
- [37] Araña, J.; Doña-Rodríguez, J.M.; Garriga I Cabo, C.; González-Díaz, O.; Herrera-Melián, J.A.; Pérez-Peña, J. FTIR study of gas-phase alcohols photocatalytic degradation with TiO<sub>2</sub> and AC-TiO<sub>2</sub>. *Appl. Catal. B* 2004, 53, 221-232.
- [38] Selvakumar, S.; Nuns, N.; Trentesaux, M.; Batra, V.S.; Giraudon, J.-M.; Lamonier, J.-F. Reaction of formaldehyde over birnessite catalyst: A combined XPS and ToF-SIMS study, *Appl. Catal. B* 2018, 223, 192-200.
- [39] Zhang, J.; Li, Y.; Wang, L.; Zhang, C.; He, H. Catalytic oxidation of formaldehyde over manganese oxides with different crystal structures. *Catal. Sci. Technol.* 2015, 5, 2305-2313.

- [40] Hartel, P.; Rose, H.; Dinges, C. Conditions and reasons for incoherent imaging in STEM. *Ultramicroscopy* 1996, 63, 93-114.
- [41] Yuan, Q.; Wu, Z.; Jin, Y.; Xu, L.; Xiong, F.; Ma, Y.; Huang, W. Photocatalytic cross-coupling of methanol and formaldehyde on a rutile TiO<sub>2</sub> (110) surface. *J. Am. Chem. Soc.* 2013, 135, 5212-5219.
- [42] Wang, J.; Li, J.; Jiang, C.; Zhou, P.; Zhang, P.; Yu, J. The effect of manganese vacancy in birnessite-type MnO<sub>2</sub> on room-temperature oxidation of formaldehyde in air. *Appl. Catal. B* 2017, 204, 147-155.
- [43] Zhu, X.; Cheng, B.; Yu, J.; Ho, W. Halogen poisoning effect of Pt-TiO<sub>2</sub> for formaldehyde catalytic oxidation performance at room temperature. *Appl. Surf. Sci.* 2016, 364, 808-814.
- [44] Wang, Z.; Chen, B.; Crocker, M.; Yu, L.; Shi, C. New insights into alkaline metal modified CoMn-oxide catalysts for formaldehyde oxidation at low temperatures. *Appl. Catal. A* 2020, 596, 117512.

## Figure Captions

**Figure 1.** XPS core level spectra of (a) Mn 3s and (b) O 1s of LMO and the A-site substituted perovskites.

**Figure 2.** EPR spectra of LMO (black) and LNMO (red).

**Figure 3.** H<sub>2</sub>-TPR profiles of LMO and the A-site substituted perovskites.

**Figure 4.** O<sub>2</sub>-TPD profiles of (a) LMO, (b) LSMO, (c) LNMO and (d) LKMO, followed by simultaneous MS on-line detection with m/z = 32 assigned to O<sub>2</sub> in the gas phase.

**Figure 5.** Catalytic oxidation of HCHO over (a) LMO and the A-site substituted perovskites: (b) LSMO, (c) LNMO, and (d) LKMO (C<sub>HCHO</sub> = 100 ppm, 20 vol% O<sub>2</sub>, He balance, RH = 0 %, GHSV = 30 L.g<sub>catal</sub><sup>-1</sup>.h<sup>-1</sup>).

**Figure 6.** *In situ* EPR spectra of HCHO-saturated (a) LMO and (b) LNMO samples gradually heated over 550 K. Insert: superimposed spectra of (black) the initial material at RT, (red) after heating to 550 K, and (blue/green) after cooling down to RT.

**Figure 7.** (a-b) HR HAADF images of the LNMO sample after HCHO stability test in anhydrous environment. (c)-(f) STEM-EDX maps of La, Mn, Na and O for the same area. The HAADF image are taken in the [130] zone axis. The atomic rows with highest intensity correspond to La columns (green arrow), lower intensity rows correspond to Mn columns (red arrow). The black arrows indicate places of mixed atomic columns with mixed Na/La character.

**Figure 8.** Effect of moisture on HCHO conversion with time on stream over (a) LNMO at 123 °C and (b) LKMO at 108 °C (C<sub>HCHO</sub> = 100 ppm, 20 vol% O<sub>2</sub>, He balance, RH = 46 %, GHSV = 30 L.g<sub>catal</sub><sup>-1</sup>.h<sup>-1</sup>).

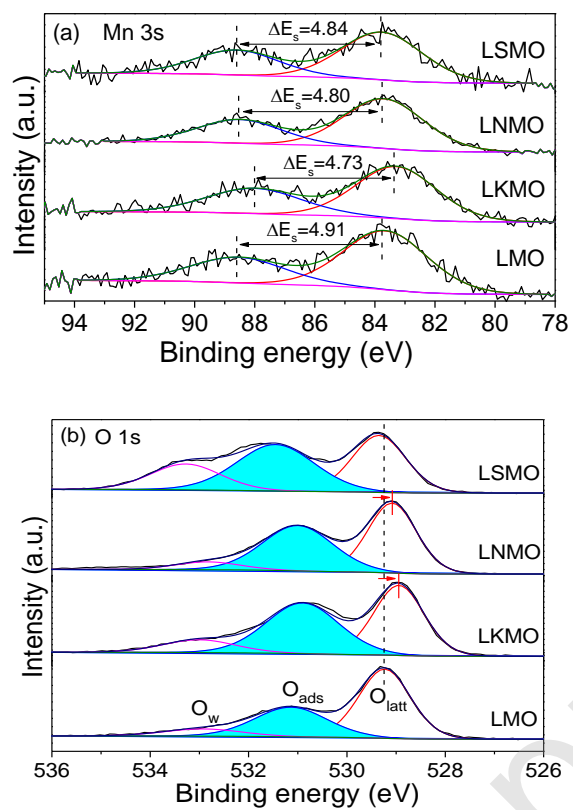


**Figure 1.** XPS core level spectra of (a) Mn 3s and (b) O 1s of LMO and the A-site substituted perovskites.

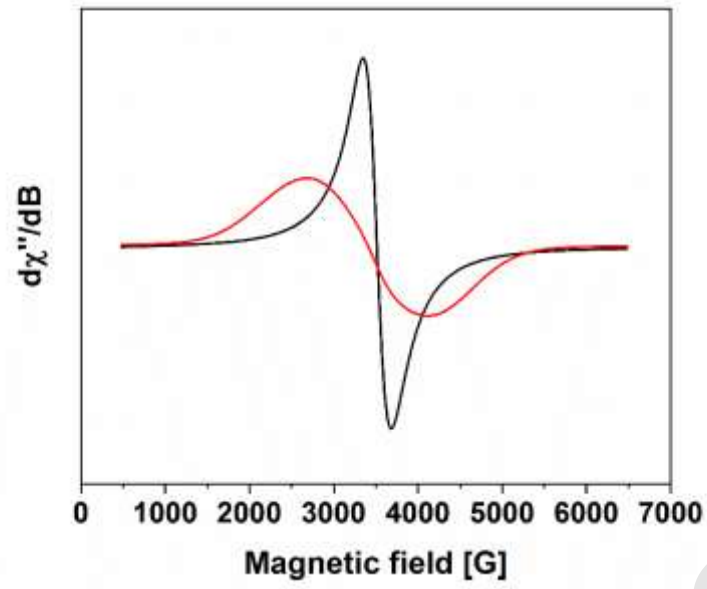


**Figure 2.** EPR spectra of LMO (black) and LNMO (red).

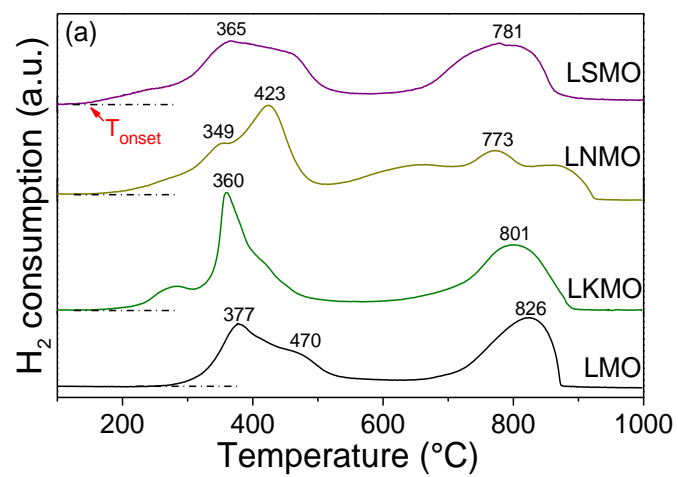


**Figure 3.** H<sub>2</sub>-TPR profiles of LMO and the A-site substituted perovskites.

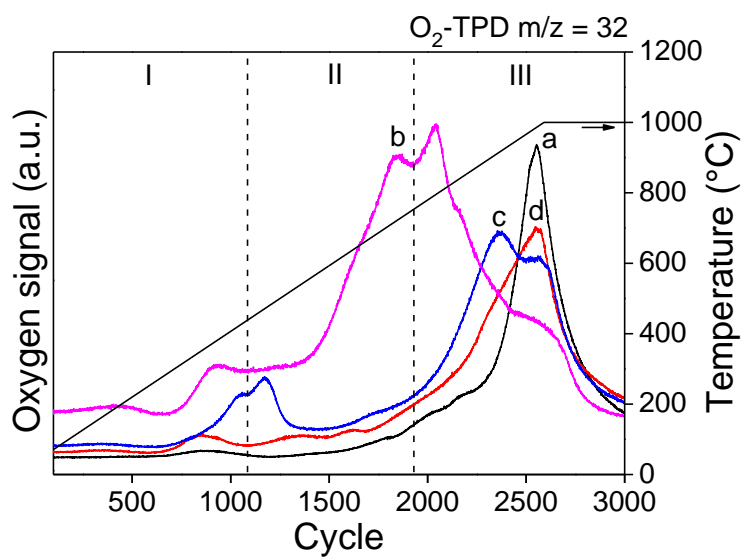


**Figure 4.** O<sub>2</sub>-TPD profiles of (a) LMO, (b) LSMO, (c) LNMO and (d) LKMO, followed by simultaneous MS on-line detection with m/z = 32 assigned to O<sub>2</sub> in the gas phase.

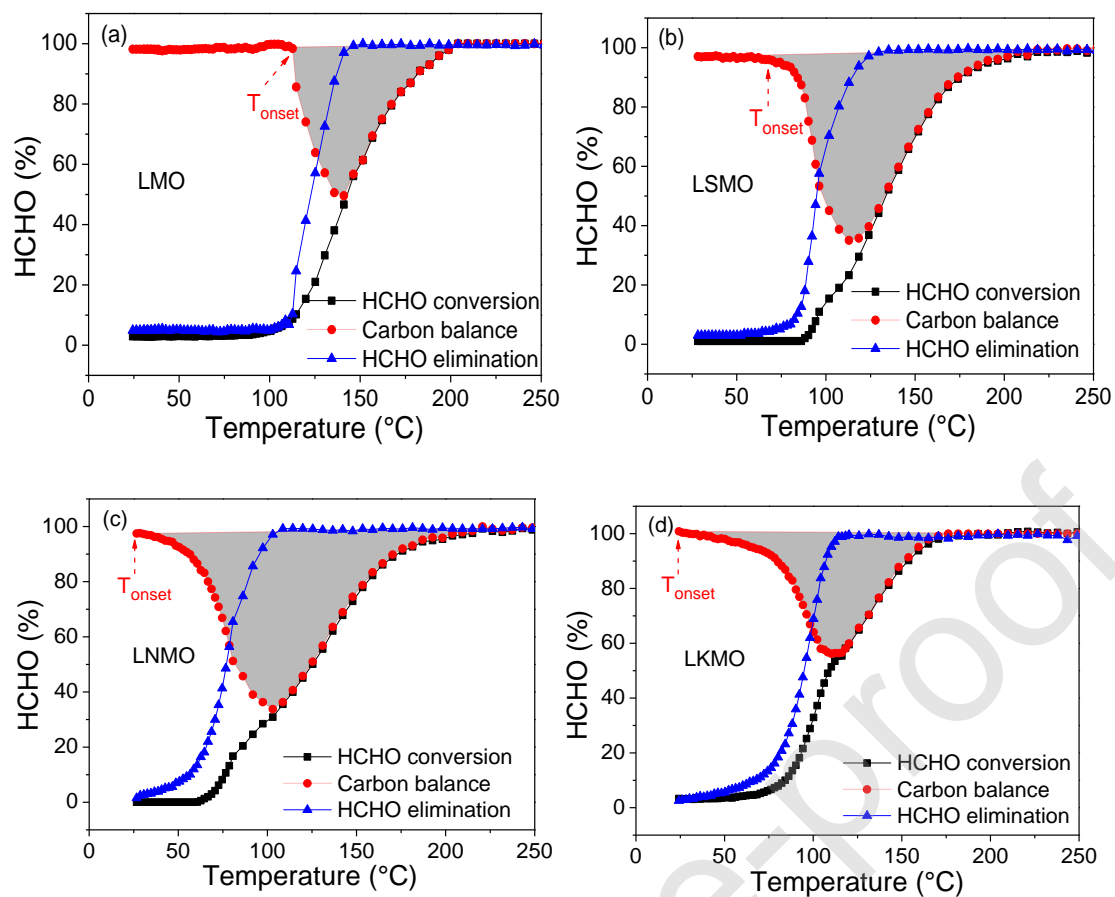


**Figure 5.** Catalytic oxidation of HCHO over (a) LMO and the A-site substituted perovskites: (b) LSMO, (c) LNMO, and (d) LKMO ( $C_{\text{HCHO}} = 100$  ppm, 20 vol%  $\text{O}_2$ ,

He balance, RH = 0 %, GHSV = 30  $\text{L}\cdot\text{g}_{\text{catal}}^{-1}\cdot\text{h}^{-1}$ ).

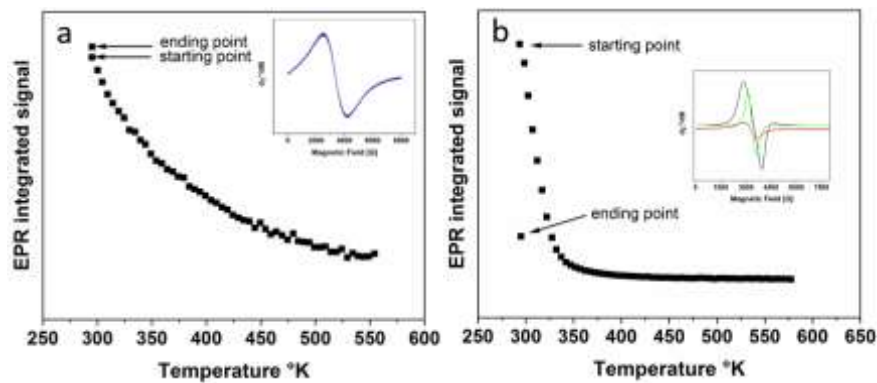


**Figure 6.** *In situ* EPR spectra of HCHO-saturated (a) LMO and (b) LNMO samples gradually heated over 550 K. Insert: superimposed spectra of (black) the initial material at RT, (red) after heating to 550 K, and (blue/green) after cooling down to RT.

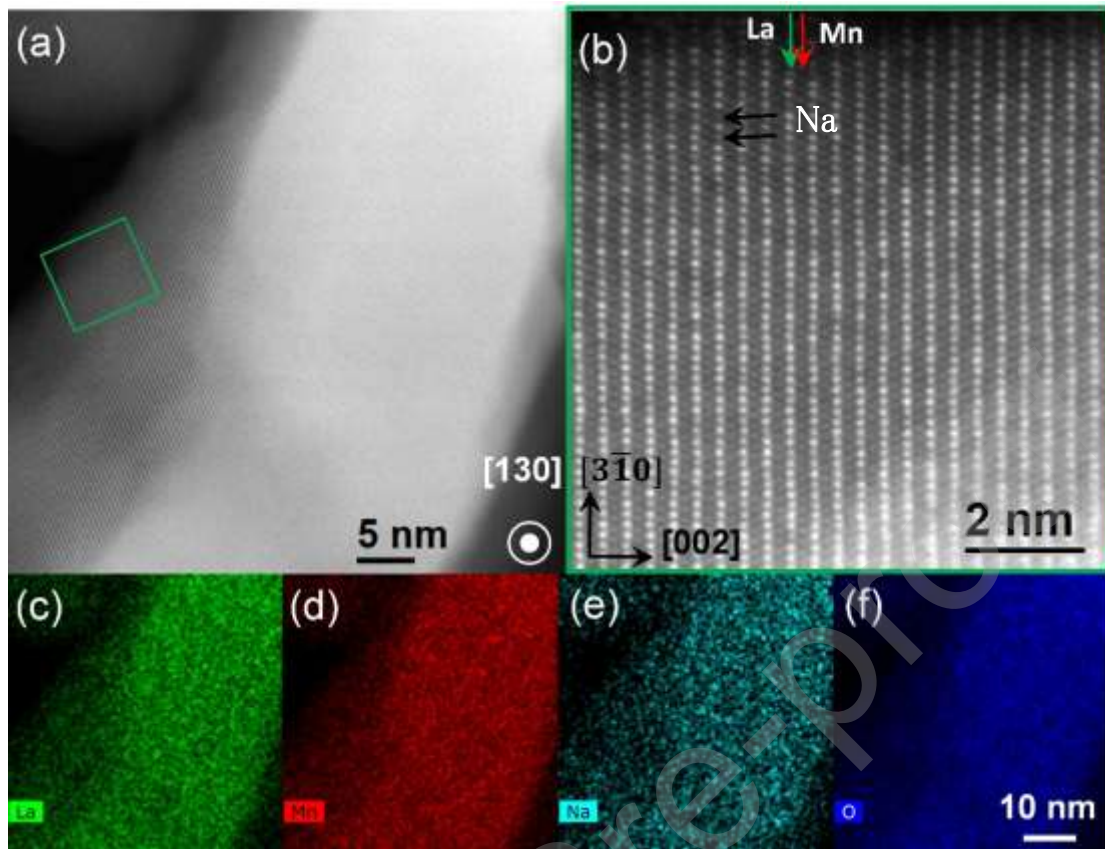


**Figure 7.** (a-b) HR HAADF images of LNMO after HCHO stability test in anhydrous environment. (c)-(f) STEM-EDX maps of La, Mn, Na and O for the same area. The HAADF image are taken in the  $[130]$  zone axis. The atomic rows with highest intensity correspond to La columns (green arrow), lower intensity rows correspond to Mn columns (red arrow). The black arrows indicate places of mixed atomic columns with mixed Na/La character.

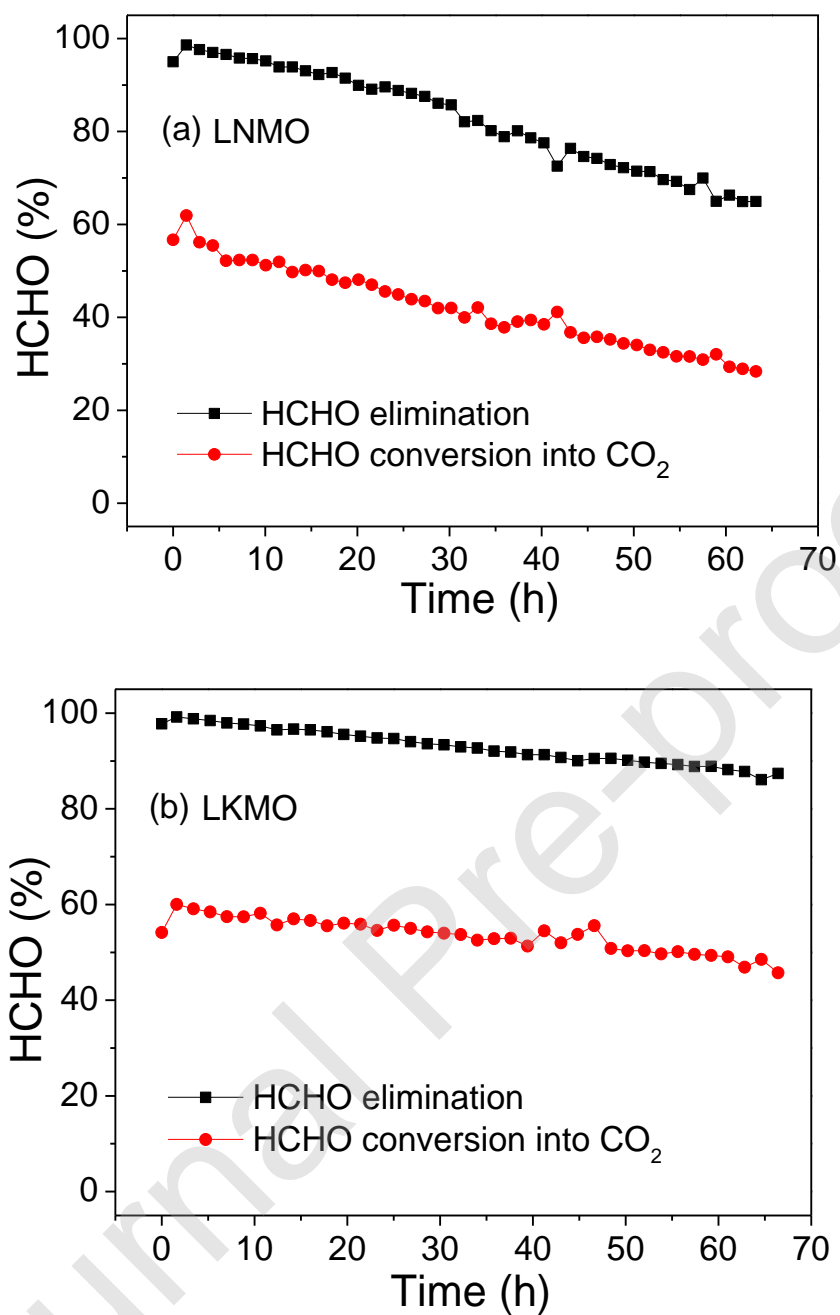


**Figure 8.** Effect of moisture on HCHO conversion with time on stream over (a) LNMO and (b) LKMO ( $C_{\text{HCHO}} = 100$  ppm, 20 vol% O<sub>2</sub>, He balance, RH = 46 %, GHSV = 30 L.g<sub>catal</sub><sup>-1</sup>.h<sup>-1</sup>).

**Table 1.** Relative surface abundance of the elements constituting LMO and the A-site substituted perovskites.

Samples	A/Mn <sup>a</sup>		La/Mn <sup>a</sup>	A/La <sup>a</sup>	Mn/(La+A+Mn) <sup>a</sup>	AOS (Mn) <sup>b</sup>	O <sub>ads</sub> /O <sub>tot</sub>
	ICP	XPS	XPS	XPS	XPS	XPS	XPS
LMO	-	-	1.1 (1.0)	-	0.5 (0.50)	3.4	0.34
LKMO	0.20 (0.20)	0.4 (0.20)	1.1 (0.8)	0.3 (0.25)	0.4 (0.50)	3.6	0.46
LNMO	0.30 (0.20)	0.6 (0.20)	1.2 (0.8)	0.5 (0.25)	0.4 (0.50)	3.6	0.45
LSMO	0.19 (0.20)	0.2 (0.20)	0.9 (0.8)	0.2 (0.25)	0.5 (0.50)	3.5	0.43

<sup>a</sup> Data in brackets are the nominal compositions of the reference and modified LMO samples.

<sup>b</sup> Margin of error  $\pm 10\%$

**Table 2.** H<sub>2</sub> consumption deduced from H<sub>2</sub>-TPR for LMO and the A-site substituted perovskites.

Samples	H <sub>2</sub> consumption (mmol/g)				Total
	Low T		Low temperature range	High T	
	(<315 °C)	(315-600 °C)			
LMO	0.04	1.33	1.37	1.29	2.66
LKMO	0.31	1.36	1.67	1.33	3.00
LNMO	0.19	1.44 <sup>a</sup>	1.63	1.33 <sup>a</sup>	2.96
LSMO	0.19	1.39	1.58	1.27	2.85

<sup>a</sup> Data in low T and high T are calculated on 315-500 °C and 500-1000 °C, respectively.

**Table 3.** Catalytic activity of LMO and the A-site substituted perovskites for HCHO oxidation.

Samples	HCHO conversion temperature (°C)			
	T <sub>10</sub>	T <sub>50</sub>	T <sub>90</sub>	T <sub>onset</sub>
LMO	114	145	185	112
LKMO	84	108	153	25
LNMO	76	123	167	25
LSMO	96	133	175	68